Available online at www.sciencedirect.com
ScienceDirect
Dyes and Pigments 78 (2008) 39–47
DYES and PIGMENTS
www.elsevier.com/locate/dyepig

Methyl orange degradation over a novel Bi-based photocatalyst Bi_3SbO_7: Correlation of crystal structure to photocatalytic activity

Xinping Lin, Fuqiang Huang*, Wendeng Wang, Zhichao Shan, Jianlin Shi

State Key Laboratory of High Performance Ceramics and Superfine Microstructures, Shanghai Institute of Ceramics, Chinese Academy of Sciences, 1295 Ding Xi Road, Shanghai 200050, PR China

Received 24 April 2007; received in revised form 11 October 2007; accepted 16 October 2007
Available online 22 October 2007

Abstract

Bi_3SbO_7 was synthesized by a solid state reaction method and the as-synthesized powder was characterized by X-ray diffraction (XRD) and UV–vis diffuse reflectance spectrum. The photocatalytic activity of Bi_3SbO_7 was evaluated by means of the degradation of methyl orange; the effects of photocatalyst concentration, pH and wavelength of irradiation upon photocatalytic performance were investigated. The photocatalytic character of Bi_3SbO_7 was discussed in terms of band structure and crystal structure. The results obtained reveal that Bi_3SbO_7 has an intrinsic optical band gap of 2.71 eV and can photocatalytically respond to light upto ~600 nm. Generally, Bi_3SbO_7 shows better photocatalytic activities than $BiVO_4$ under both UV and visible light because of the lower packing factor and correspondingly higher structural openness of Bi_3SbO_7.

Keywords: Photocatalysis; Methyl orange; Bi_3SbO_7; $BiVO_4$; Packing factor

1. Introduction

Photocatalysis has attracted increasing attention since Fujishima and Honda announced a TiO_2 photochemical electrode for splitting water in 1972 [1]. The technique is regarded as one of the most promising solutions to the severe problems of energy shortages and environment crises recently existing in the world. As an efficient and commercially cheap photocatalyst, titanium dioxide (TiO_2) has been intensively studied, especially in the field of organic contaminant purification. However, the semiconductor is a wide band gap material with E_g of about 3.20 eV. It means that TiO_2 catalyst works only under the UV light, whose energy occupies about 4% in the sunlight spectrum. To achieve a visible-light-responsive ability of a semiconductor is a practically important object for photocatalysis. Besides the focused works on TiO_2 modification, many efforts were made to develop other efficient visible-light-driven photocatalysts.

Recently, Bi(III)-based oxide compounds are of particular interest as visible-light-driven photocatalysts. In these materials, the conduction band minimum (CBM) includes Bi 6p orbitals and the valence band maximum (VBM) contains Bi 6s and O 2p orbitals. Thus, Bi-based oxide semiconductors are easy to acquire a visible-light-responsive ability due to the similar band structure to Bi_2O_3. The typical efficient Bi-based photocatalysts are $BiVO_4$ [2–5], $CaBi_2O_4$ [6], $SrBi_2O_4$ [7], Bi_2WO_6 [8,9], Bi_2MoO_6 [10], bismuth titanium oxides [11–13], γ-Bi_2O_3 [14–16] and some Bi-based multiple-metal oxides [17–19]. In the present paper, we report another novel Bi-based photocatalyst that to the best of our knowledge has not yet been studied for this purpose, Bi_3SbO_7, for degrading methyl orange. The semiconductor with an optical band gap of 2.71 eV shows a fair visible-light-responsive photocatalytic activity. Generally, Bi_3SbO_7 exhibits much better photocatalytic performances than the extensively researched catalyst $BiVO_4$ under UV light and visible light illuminations. The activity difference of Bi_3SbO_7 and $BiVO_4$ was mainly discussed in close connection with crystal structural properties, and the lower packing factor corresponding to the higher structural

* Corresponding author. Tel.: +86 21 52411620; fax: +86 21 52413903.
E-mail address: huangfq@mail.sic.ac.cn (F. Huang).

0143-7208/$ - see front matter © 2007 Elsevier Ltd. All rights reserved.
doi:10.1016/j.dyepig.2007.10.005

openness degree of Bi_3SbO_7 can account for its higher photocatalytic performance.

2. Experimental

The polycrystalline Bi_3SbO_7 powder was synthesized by a solid state reaction method. Bi_2O_3 (Sinoreg, 99.5%) and Sb_2O_3 (Sinoreg, 99.5%) were used as starting raw materials. The blended reagents with the stoichiometric proportion were calcined at 820 °C in air for 12 h, with intermediate grindings. The photocatalytic reference, $BiVO_4$, was synthesized at a lower temperature, 700 °C for 12 h, using Bi_2O_3 and V_2O_5 (Sinoreg, 99.5%) as raw materials. The as-prepared powders were characterized by X-ray diffraction (XRD) and UV–vis diffuse reflection spectrum.

Analytical-grade disazo acid dye, Methyl Orange 52 (C.I. 13025), with the chemical formula of $C_{14}H_{14}N_3NaO_3S$ and the molar mass of 327.34, was used for degradation to investigate the photocatalytic activity of Bi_3SbO_7 (for simplicity, the acid dye was denoted as MO in the following context). The photocatalytic reactor consists of two parts, a quartz cell with a circulating water jacket and a 500 W high-pressure mercury lamp with a maximum emission at 365 nm placed inside the quartz cell. In all experiments, the reaction temperature was kept at room temperature to prevent any thermal catalytic effect by using the circulating water jacket. Before photocatalytic reaction, a certain mass of catalyst powder was added in 300 ml MO solution with a concentration of 10 mg/l. The solutions of NH_4OH (1.0 mol/l) and H_2SO_4 (1.0 mol/l) were used to adjust the pH value of MO solution. UV illumination was conducted after the suspension was magnetically stirred in the dark for 50 min to reach the adsorption–desorption equilibrium of MO on catalysts. During irradiation, about 5 ml suspension was continually taken from the reaction cell at given time intervals for the subsequent MO concentration analysis after centrifuging. The MO degradation was calculated by the following equation:

$$\eta = (C_0 - C)/C_0 = (A_0 - A)/A_0 \quad (1)$$

where C_0 and A_0 are the initial concentration and absorbance of methyl orange solution at 464 nm corresponding to maximum absorption wavelength after equilibrium adsorption of the dye; C and A are the concentration and absorbance of methyl orange solution at 464 nm after UV light illumination.

3. Results and discussion

3.1. XRD patterns and UV–vis diffuse reflectance spectra of as-synthesized powders

The as-synthesized Bi_3SbO_7 appears reddish yellow with a BET surface area of 0.11 m^2/g, and its phase with a triclinic structure was confirmed by XRD analysis, as shown in Fig. 1. The UV–vis diffuse reflectance spectra of as-synthesized powders are shown in Fig. 2. The optical absorption of Bi_3SbO_7 starts at about 600 nm and the absorbance sharply

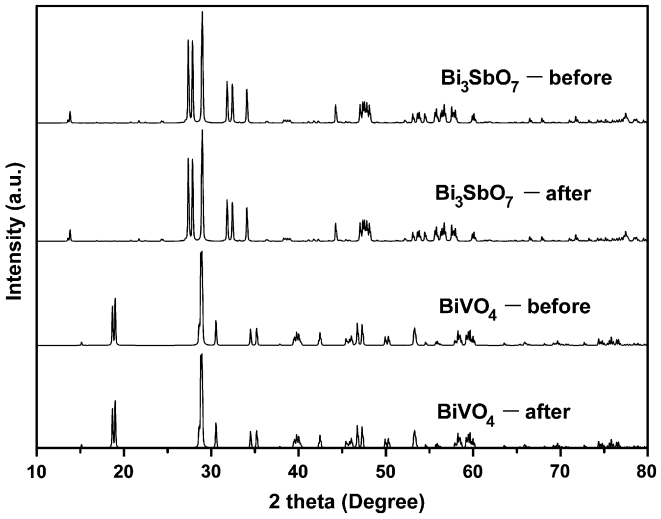

Fig. 1. XRD patterns of Bi_3SbO_7 and $BiVO_4$ before and after photocatalytic reactions.

increases below about 460 nm. The intrinsic absorption edge was determined at 458 nm and the corresponding band gap is 2.71 eV. It is of interest that the optical absorption start, about 600 nm, is obviously longer than the intrinsic absorption edge (458 nm). This means that the material can photocatalytically respond to the light wavelength extending to as long as about 600 nm, which will be experimentally proved in the following context.

In our experiment, the extensively studied, efficiently visible-light-responsive photocatalyst, $BiVO_4$, was used as a photocatalytic reference to qualitatively understand the photocatalytic performance of Bi_3SbO_7. The as-synthesized monoclinic $BiVO_4$ powder is red in color with the BET surface area of 0.18 m^2/g. Its optical band gap was determined as 2.30 eV. Both Bi_3SbO_7 and $BiVO_4$ have an optical absorption start at about 600 nm though their band gaps are different. Such a similar optical absorption property is another reason

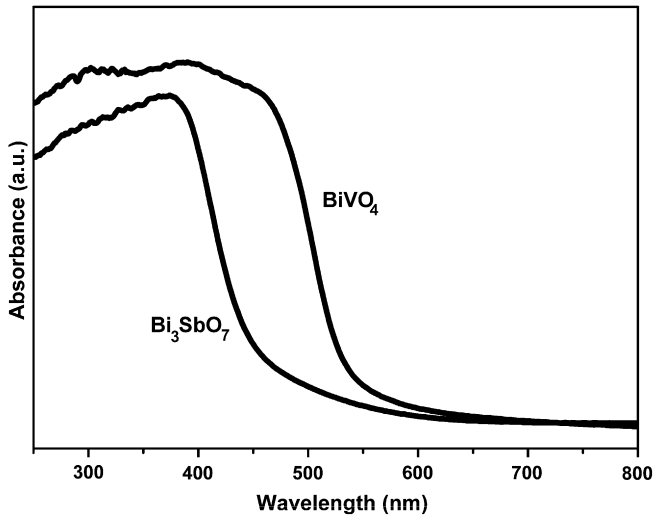

Fig. 2. UV–vis diffuse reflectance spectra of Bi_3SbO_7 and $BiVO_4$.

why $BiVO_4$ was selected as a reference in the present paper. The photophysical properties of the two semiconductors are listed in Table 1.

3.2. Band structure

Electronic structure of Bi_3SbO_7 was calculated by TB-LMTO program, which is a self-consistent, scalar relativistic linearized muffin-tin orbital program by Andersen and co-workers within the atomic sphere approximation [20–22]. This method splits the crystal space into overlapping atomic spheres (Wigner–Seitz spheres) whose radii are chosen to fill completely the crystal volume. In the present calculations, the von Barth–Hedin exchange-correlation potential was used within the local density approximation (LDA) [23]. All *k*-space integrations were performed with the tetrahedron method [24,25]. The basis sets consisted of the valence 6s and 6p states for Bi, 5s and 5p states for Sb and 2s and 2p states for O. The 6d states for Bi, 5d states for Sb and 3d states for O and p–d states for empty spheres were downfolded by means of the technique described by Löwdin [26]. Within the Brillouin zone of the cell, 260 irreducible *k*-points from 512 were used. The high-symmetry points are *B* (1/4, 1/2, 1/4), *Γ* (0, 0, 0) and *Z* (0, 0, 1/2) in terms of the reciprocal basis vectors [27].

The band structure of Bi_3SbO_7 is displayed in Fig. 3. The lowest unoccupied state lies at the *B* point, while the highest occupied state is at the *Γ* point. This means Bi_3SbO_7 is an indirect gap material. Fig. 4 shows the partial and total states of densities (DOS) of Bi_3SbO_7. The bands just below the Fermi level are mainly localized O 2p and Bi 6s orbitals, in which Bi 6s makes a less contribution to VBM; the bands at 2.7–5 eV above the Fermi level consisting of Bi 6p, Sb 5s and O 2p (anti-bonding states of Bi–O and Sb–O) are much more dispersed. In other words, CBM is mainly composed of Bi 6p and Sb 5s orbitals; VBM primarily consists of O 2p and Bi 6s orbitals. The calculated band gap is 2.73 eV, which is in good agreement with the experimentally measured value of 2.71 eV. The hybrid states that can lead to the fair dispersions in the conduction and valence bands of Bi_3SbO_7, which may also imply a fair mobility of photogenerated charges to travel a long distance, assisting the photostimulated electron-hole separation and improving the photocatalytic activity of the compound.

3.3. Photocatalytic activity

3.3.1. Effect of powder concentration in suspension

Methyl orange, a kind of chemically stable and difficultly decomposed dye, was presently adopted as a representative organic pollutant to evaluate the photocatalytic activity of

Table 1
Band gaps, optical absorption starts (λ_s), BET surface areas and the pseudo-first UV-induced photocatalytic reaction rates (k) of as-prepared Bi_3SbO_7 and $BiVO_4$

Catalyst	E_g (eV)	λ_s (nm)	BET (m^2/g)	k (min^{-1})
Bi_3SbO_7	2.71	600	0.11	0.016
$BiVO_4$	2.30	600	0.18	0.0016

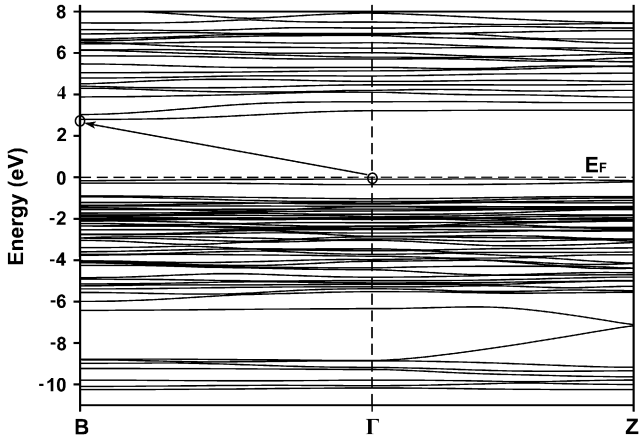

Fig. 3. Band structure of Bi_3SbO_7, where the labels are *B* (1/4, 1/2, 1/4), *Γ* (0, 0, 0) and *Z* (0, 0, 1/2).

Bi_3SbO_7. Fig. 5 illustrates the UV–vis light absorption spectrum of MO aqueous solution under neutral condition with the initial concentration of 10 mg/l. There are two absorption maxima in the spectrum. The first band was observed at 271 nm and the second band at 464 nm. The band at 464 nm that is associated with the azo bond (–N=N–) was used to monitor the effect of the photocatalysis on the degradation of MO under neutral conditions.

Fig. 6 indicates the influence of Bi_3SbO_7 powder concentration in suspension on MO decomposition. It can be seen that the MO dye shows rather chemical stability, and the MO photolysis upon UV light irradiation in the blank experiment is unobservable. An increase of the catalyst concentration within the selected experiments results in an improvement of the photocatalytic efficiency. After 100 min of UV light irradiation, MO removal in the suspension with the photocatalyst concentration of 0.05 g/100 ml is only 32.2%, and obviously rises to 69.3% at 0.1 g/100 ml. The MO decolorization behaviors as a function of UV irradiation time are much close as the loading

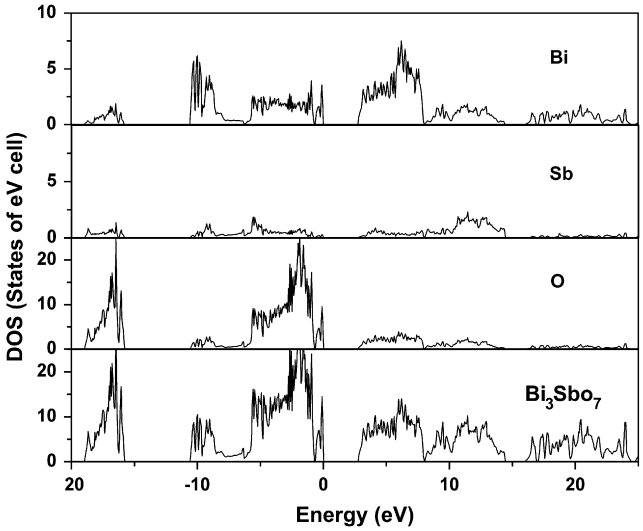

Fig. 4. Partial and total DOS of Bi_3SbO_7.

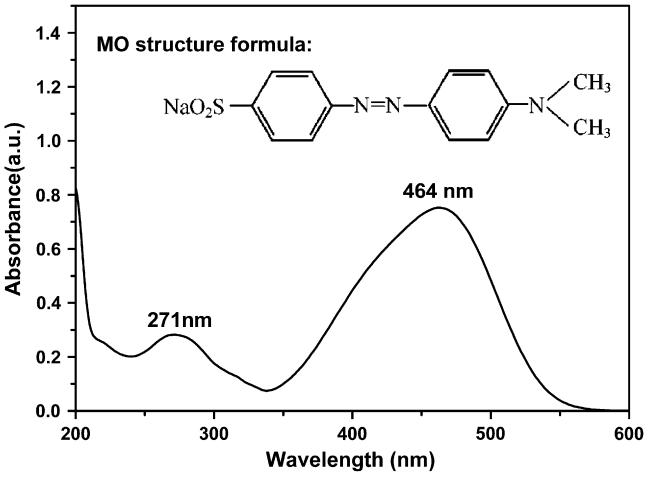

Fig. 5. UV–vis light absorption spectrum of the initial MO solution with 10 mg/l.

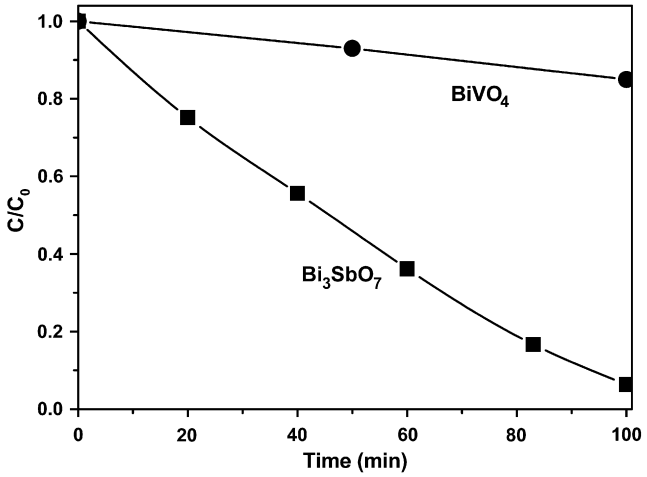

Fig. 7. Comparison of photocatalytic activities between Bi_3SbO_7 and $BiVO_4$.

concentration increases to 0.2, 0.3 and 0.4 g/100 ml. Such a slowed-down enhancement in the photocatalytic efficiency as the concentration increases from 0.05 g/100 ml to 0.4 g/100 ml mainly results from the contradiction or mutual competition between the larger photocatalytically activated surface and the stronger light reflection on the photocatalyst powder.

Fig. 7 gives the comparison of photocatalytic activities of Bi_3SbO_7 and $BiVO_4$. The added concentrations of the two catalysts in suspensions are both 0.2 g/100 ml. The equilibrium adsorptions of MO on Bi_3SbO_7 and $BiVO_4$ are 3.1% and 4.2% before the photocatalytic reactions, which are in good agreement with their surface area difference. The slight difference of the two initial equilibrium adsorptions is believed not to affect the subsequent comparative discussion on the discrepancy of intrinsic photocatalytic efficiencies of the two materials. It can be seen that Bi_3SbO_7 shows a much better property than the extensively researched photocatalyst $BiVO_4$. The MO decolorization over $BiVO_4$ after 100 min UV light illumination is merely 15.0%, obviously lower than 93.7% over Bi_3SbO_7. In order to quantitatively understand the reaction rates of the MO degradations over the two materials, we applied the pseudo-first order model as expressed by Eq. (2), which is generally used for photocatalytic degradation process if the initial concentration of pollutant is low [28],

$$\ln(C_0/C) = kt \tag{2}$$

where C_0 and C are the concentrations of dye in solution at time 0 and t, respectively, and k is the pseudo-first order rate constant. The pseudo-first order rate constant k of Bi_3SbO_7 is 0.016 min^{-1} ($R = 98.4\%$), about 10 times as high as 0.0016 min^{-1} ($R = 98.8\%$) of $BiVO_4$ (see Table 1).

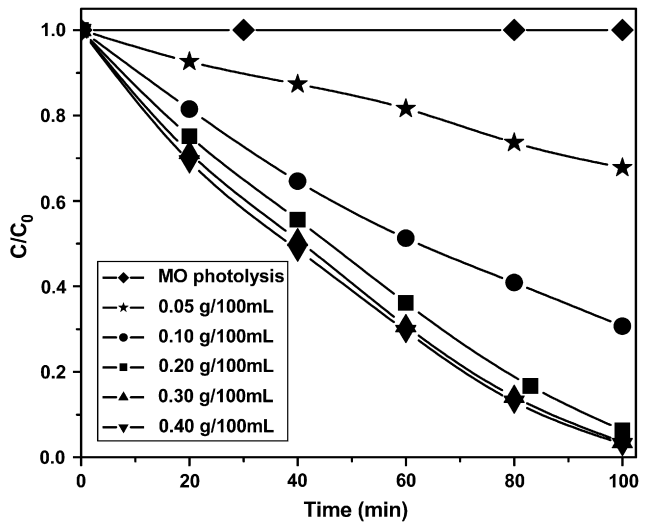

Fig. 6. Effect of powder concentration in suspension on the photocatalytic efficacy.

3.3.2. Effect of pH value of suspension

Fig. 8 shows the pH-dependent photocatalytic activities of Bi_3SbO_7 under UV light irradiation. There are no phase variations detected by XRD analysis after any of the selected experiments in acidic conditions. The pH value shows a strong influence on the MO photodegradation. The photodegradation efficacy rises with the decreasing pH value. The reaction rate constants (k) are 0.010 (pH 8.5), 0.016 (pH 6.9), 0.027 (pH 5.5), 0.054 (pH 4.5), 0.074 (pH 3.5) and 0.094 min^{-1} (pH 3.0), respectively. The pH-dependent photodecomposition can be mainly attributed to the variation of surface charge properties of the photocatalyst at different pH values. Consequently, this changes the absorption behavior of a dye on a catalyst surface. Since MO is an anionic dye, its adsorption is favored in the acidic solution, as shown in Fig. 9. The increasing amount of MO in close contact with the catalyst spatially facilitates its oxidative degradation primarily by positive holes or hydroxyl radicals upon photoexcitation [7]. On the other hand, MO becomes unstable in acidic conditions, the λ_{max} of MO, which is commonly measured by the energy required for decomposing dye molecular structure, increases from 464 nm to 506 nm with the pH value decreasing from 6.9 to 3.0. This also makes the decolorization easier.

3.3.3. Visible-light-induced photocatalysis

As stated above, Bi_3SbO_7 with the band gap of 2.71 eV has an optical absorption start at 600 nm or so. Thus, it is expected

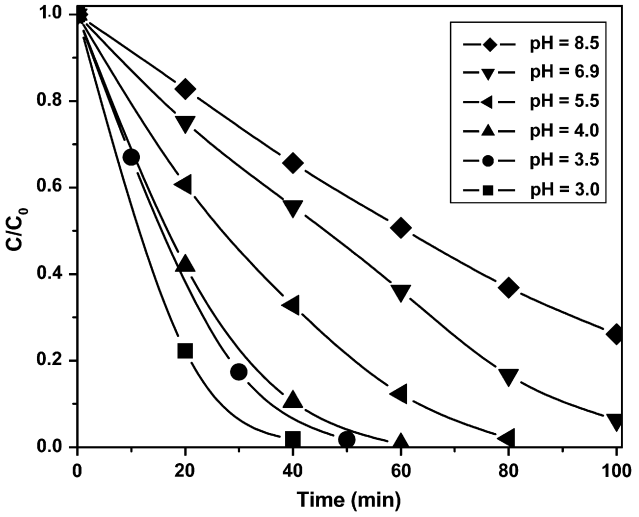

Fig. 8. pH-dependent photocatalytic activities over Bi_3SbO_7.

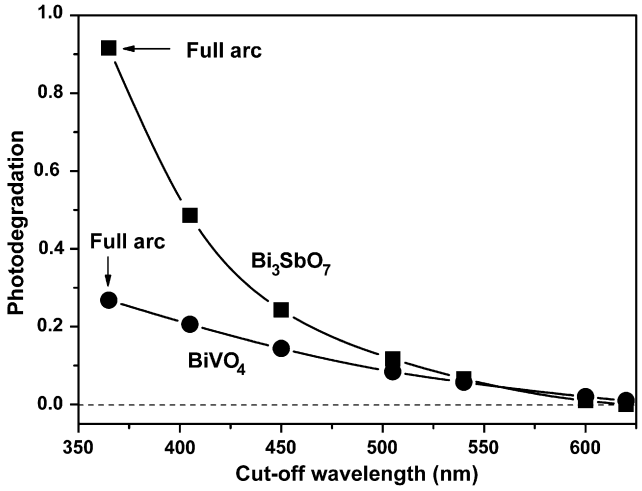

Fig. 10. Cut-off wavelength-dependent photocatalytic activities of Bi_3SbO_7 and $BiVO_4$.

that the material possesses a fair photocatalytic activity under visible light. In order to confirm the visible-light-induced photocatalysis, a 500 W Xe lamp cut by light filters was used for illumination. The cut-off wavelength-dependent photocatalytic properties over Bi_3SbO_7 and $BiVO_4$ are shown in Fig. 10, in which the irradiation times for the two catalysts at different cut-off wavelengths are all 180 min. Generally, Bi_3SbO_7 shows a better visible-light-responsive photocatalytic activity than $BiVO_4$. Under the typical visible light ($\lambda > 405$ nm), the MO decolorization over Bi_3SbO_7 is 48.6%, higher than 20.6% over $BiVO_4$. Though the intrinsic absorption edge of Bi_3SbO_7 is 458 nm, the material can still photocatalytically respond to the photons with a much longer light wavelength extending to about 600 nm. Under the visible light with the wavelength longer than 550 nm, Bi_3SbO_7 is still more photocatalytically active than $BiVO_4$.

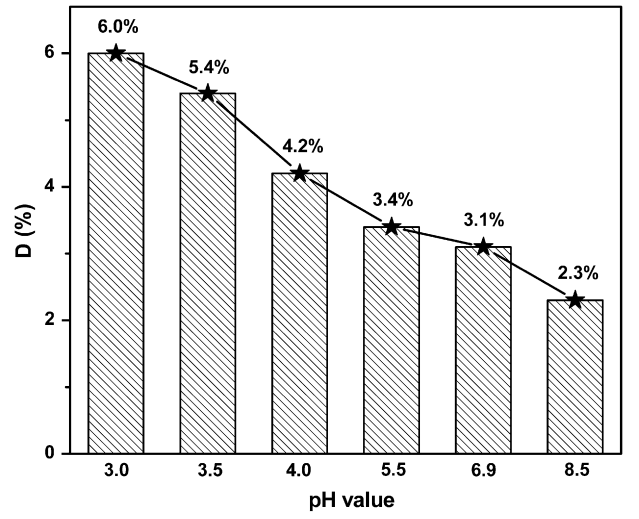

Fig. 9. pH-dependent equilibrium adsorption of MO over Bi_3SbO_7. $D = (C_0 - C)/C_0 \times 100\%$, where C_0 is the initial MO concentration and C is the concentration after equilibrium adsorption.

It is widely accepted that there are three possible mechanisms [29,30] for the degradation of a dye, a photocatalytic process, a dye photosensitization process and a photolysis process. For the photocatalytic process, photoinduced electrons or holes emerging over a semiconductor directly or indirectly react with O_2 and OH^- to form $\bullet O_2^-$ and •OH oxidative species. For the dye photosensitization, photoinduced electrons in the dye transfer to the conduction band of the catalyst that absorbs the dye, and subsequently reacts with molecular oxygen to produce the $\bullet O_2^-$ oxidative species [29]. For the dye photolysis, it is originated from the destruction of a dye upon photoirradiation, which is closely related to the structure stability of the dye. The main mechanism for the dye photolysis is that a photoinduced electron on the dye directly functions with O_2 to produce a singlet oxygen atom O (^{1}D) that can work as an oxidant for the pure dye's photolysis [30].

In our experiment, the MO degradation in the blank experiment under UV light is not observable, as shown in Fig. 6. This means that MO shows high structural stability, thus, the MO decomposition by the photolysis mechanism is neglectable. In other words, the MO degradation is possibly initiated by a photocatalytic process and a dye photosensitization process. In order to investigate the role of photosensitization mechanism in the whole dye decolorization, the results of cut-off wavelength-dependent photocatalytic activity was discussibly applied. As mentioned above, the photosensitization mechanism works only as the energy of irradiation light can stimulate the dye to form photoinduced electrons that transfer to catalyst surfaces and subsequently react with the surrounding media, and the required lowest energy to stimulate MO is 464 nm (see Fig. 5). It is found from Fig. 10 that Bi_3SbO_7 can still photodegrade MO as the cut-off wavelength extends to the value longer than 464 nm. This means that the MO degradation over Bi_3SbO_7 under the wavelength region of $\lambda > 464$ nm is dominantly initiated by a photocatalytic process. Under the light of $\lambda < 464$ nm whose energy can excite MO to form photoinduced electrons, the MO degradation as a function of cut-off wavelength is closely similar to the

wavelength-dependent absorbance in the UV–vis diffuse reflectance spectrum of Bi_3SbO_7 (see Fig. 2). That is, the MO degradation in this wavelength region initiated by a dye photosensitization mechanism is believed to be at a small scale, and the enhancement of MO decolorization is mainly caused by the increase of light absorbance of Bi_3SbO_7. Thus, we can conclude that the MO degradation under UV or visible light is mainly controlled by a photocatalytic mechanism.

In the real photocatalysis process of a semiconductor for MO degradation, it is worth mentioning that the oxidative species forming over catalyst surface decompose the dye via a pathway from intermediates to the final carbon dioxide and some inorganic products (SO_4^{2-}, NO_3^- and NH_4^+) [31], as shown in Eq. (3).

$$\bullet OH/\bullet O_2^- + MO \rightarrow \text{intermediates} \rightarrow SO_4^{2-} + NO_3^- + NH_4^+ + CO_2 + H_2O \quad (3)$$

The formation of intermediates was presumably caused by the attack of oxidative species (e.g., •OH) to MO, through two primary processes – demethylation and hydroxylation [31–36]. The possible initial intermediates as MO is attacked by •OH are shown in Fig. 11, and they will be further repeatedly combined by or reacted with the oxidative species to form other intermediates till complete ring opening.

3.4. Structure–property relationship

The as-prepared Bi_3SbO_7 has a triclinic structure, as shown in Fig. 12. One Sb^{5+} ion is coordinated with six O^{2-} ions to form a fairly geometrically regular $[SbO_6]$ octahedron. The $[SbO_6]$ octahedra are connected by sharing corners to form a chain along the *c* axis. There are no direct connections among $[SbO_6]_\infty$ chains. The Bi–O polyhedra work as a "bridge" to indirectly joint $[SbO_6]_\infty$ chains. Compared to the Sb^{5+} ion, the coordination environment of Bi^{3+} is much more complicated, and seven O^{2-} ions are coordinated to one Bi^{3+} ion. Such a complicated configuration is induced by the presence of Bi(III) $6s^2$ lone electron pair. In a $[BiO_7]$ polyhedron (see in Fig. 12), five oxygen atoms form an incomplete octahedral arrangement with one apical oxygen ion to Bi^{3+} ion at ~2.1 Å and four basal-plane oxygen ions at 2.2–2.6 Å; opposite to the nearest apical oxygen, the stereochemically active Bi $6s^2$ lone electron pair completes the distorted octahedra by extending a distance of ~1.8 Å [37,38]; the remaining two oxygen atoms are electrostatically coordinated to both sides of the $6s^2$ lone electron pair with distances of ~3.0 Å. In other words, the Bi–O local structure can be originally regarded as an octahedron, in which five Bi–O bonds and the Bi $6s^2$ lone electron pair construct the octahedron; the Bi $6s^2$ is secondly hybridized to form two longer Bi–O bonds spatially nearest to the location of electrostatically active Bi $6s^2$, in this sense, the coordination number for Bi^{3+} is 7.

Such geometrically complicated or irregular local structure in a selected $[BiO_7]$ polyhedron results in a dipole moment of ca. 5.42 D (Debye). The presence of the dipole moment can work as an accelerator for an efficient photoexcited electron-hole separation in the local structure [39–43]. Studies [44,45] have given some insights about the effect of M–O–M angle, in which M ions are photocatalytically active, on the mobility for charge migration and on the consequent photocatalytic activity of a semiconductor. Specifically, the closer the angle is to the ideal 180°, the less scattering and higher mobility of photoinduced charges occur. The Sb–O–Sb angle in the $[SbO_6]_\infty$ chain is as high as 142.8°, and the selected Bi–O–Sb angles are 137.5°, 138.4°, 139.2°, 140.0°. This means that the transportation of photoexcited charges in the crystal lattice is fairly smooth. In this way, the phenomenon that photoinduced electron-hole pairs are separated in the $[BiO_7]$ local structures and subsequently smoothly transport to particle surfaces via [Sb–O–Sb] zigzag chains can easily occur.

As proved in our experiments, Bi_3SbO_7 shows a much better photocatalytic performance than $BiVO_4$. We believe

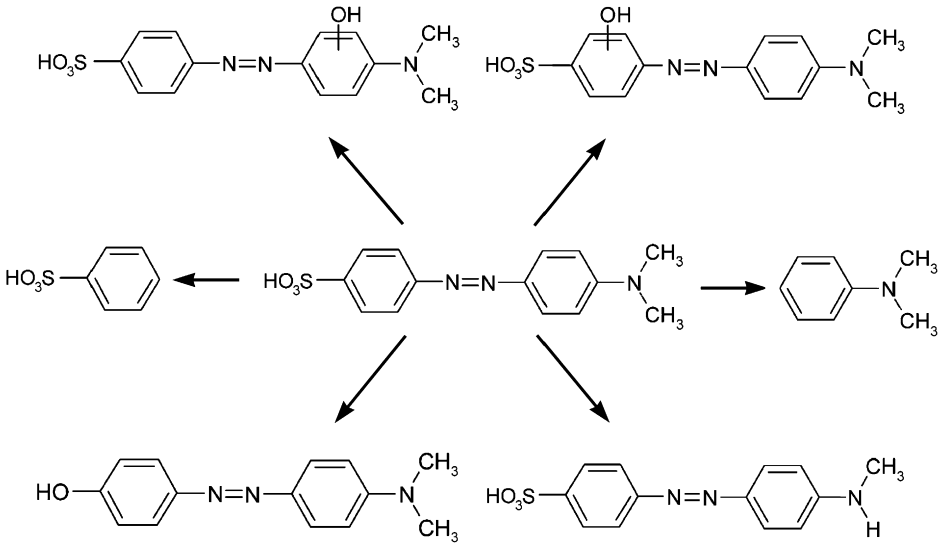

Fig. 11. Possible initial intermediates as MO is attacked by oxidative species.

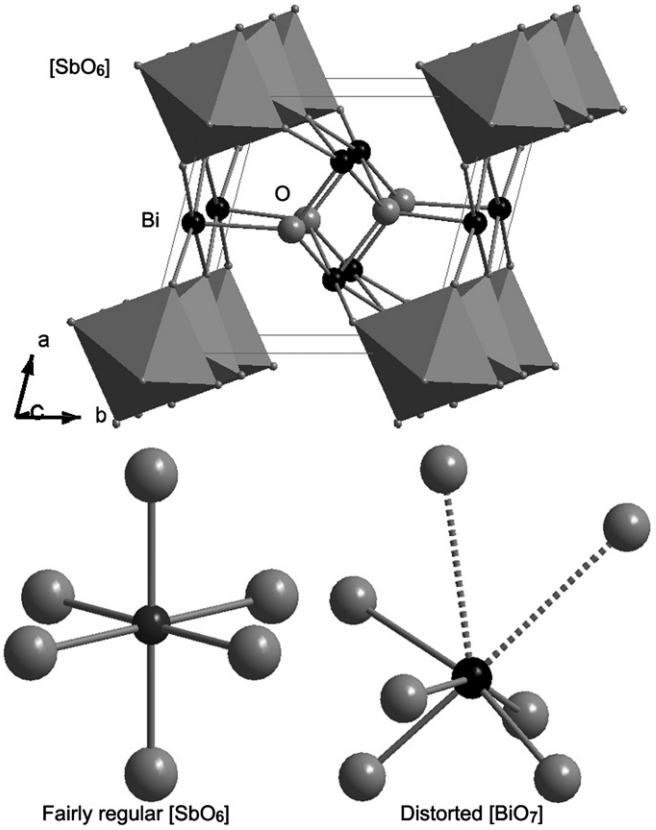

Fig. 12. Schematic diagrams of crystal structure, [SbO_6] and [BiO_7] polyhedra in Bi_3SbO_7.

that such an obvious difference in the photocatalytic activity should be in close connection with crystal structures of the two materials. The dipole moment in the distorted Bi–O polyhedra for $BiVO_4$ is ca. 1.47 D (Debye), lower than 5.42 D for Bi_3SbO_7. As far as M–O–M angles are concerned, the angles in $BiVO_4$ are generally smaller than those in Bi_3SbO_7. The V–O–V angle is as low as 104.8°, and the selected Bi–O–V angles are 129.8° and 138.6°. Thus, $BiVO_4$ should possess a lower mobility for photostimulated electron-hole separation and transportation in crystal lattice, as compared to Bi_3SbO_7.

In our previous work [46], a universal model for structure-dependent photocatalytic activity was introduced to analyze the photocatalytic difference of materials with similar band structure (similar crystal structure or chemistry), using crystal packing factor (PF) as a criterion. The model indicates that a lower packing factor, corresponding to a higher structure-openness degree, leads to a higher ability of photoinduced electron-hole separation and commonly better photocatalytic activity.

The macro-parameter, crystal packing factor, which scales the structure-openness degree of a semiconductor, to some extent can reflect the degree of micro-deformation in metal-oxygen polyhedra and/or the spatial vibration abilities of atoms in the crystal, and the consequent mobility for electron-hole separation and transportation. In this sense, our proposed structure–property relationship model may cover the idea that local structure distortion benefits electron-hole separation and the consequent photocatalytic activity. Besides, the band dispersion often associated with low PF structures may additionally increase the dispersion at the edges of conduction band minimum and valence band maximum, thus decreasing the effective mass of electrons and holes. This would further contribute to a higher mobility. These generic mechanisms may operate in a broad range of structures and at selected sites where photoelectrons and holes are generated and transported. Consequently, they could lead to wide applicability of the PF criterion.

For the two Bi-based photocatalysts (Bi_3SbO_7 and $BiVO_4$) in our experiment, they have a fairly similar band structure. That is, the conduction band minimums of the two semiconductors both include Bi 6p orbitals; the valence band maximums contain Bi 6s and O 2p orbitals. Thus, it is reasonable to apply such an above model to understand the photocatalytic difference of the two semiconductors. Packing factors of the two materials were computed by dividing the sum of spherical volumes by the unit cell volume, as seen in the following equation:

$$\mathrm{PF} = Z(xV_\mathrm{A} + yV_\mathrm{B} + zV_\mathrm{C})/V_\mathrm{cell} \tag{4}$$

where Z is the number of the formula unit in one unit cell of a semiconductor ($A_xB_yC_z$); V_A, V_B and V_C are ion volumes calculated by assuming spherical ions with a Shannon radius [47] that depends on the coordination number; and V_cell is the cell volume. The structural parameters and the calculated packing factors are listed in Table 2. The PF value of Bi_3SbO_7 is 57.9%, obviously lower than 63.9% of $BiVO_4$. In other words, the structure-openness degree of Bi_3SbO_7 is higher than that of $BiVO_4$. This means that Bi_3SbO_7 possesses a higher mobility for photoinduced electron-hole separation and transportation in the crystal lattice, which is favorable for its photocatalytic activity.

4. Conclusion

Bi_3SbO_7 synthesized by a solid state reaction method has an optical band gap of 2.71 eV. It is of interest that the material can respond to the light wavelength extending to as long as about 600 nm. It is an indirect gap material. The conduction band minimum mainly consists of Bi 6p and Sb 5s orbitals, and the valence band maximum is primarily composed of O

Table 2
Crystal structural parameters and packing factor (PF) of Bi_3SbO_7 and $BiVO_4$

Compound	Structural symmetry	Structural parameters			PF (%)
		a, b, c (Å)	α, β, γ (°)	Cell volume (Å^3)	
Bi_3SbO_7	Triclinic	$a = 6.604$ $b = 7.015$ $c = 7.605$	$\alpha = 73.39$ $\beta = 89.22$ $\gamma = 76.19$	327.3	57.9
$BiVO_4$	Monoclinic	$a = 5.197$ $b = 5.096$ $c = 11.702$	$\alpha = 90.00$ $\beta = 90.00$ $\gamma = 90.40$	309.9	63.9

2p and Bi 6s orbitals. Bi_3SbO_7 shows better photocatalytic activities than $BiVO_4$ under UV and visible light irradiations. The lower packing factor and the corresponding higher structural openness degree of Bi_3SbO_7 can account for its higher photocatalytic performance. The MO degradation over Bi_3SbO_7 is mainly initiated by a photocatalytic mechanism.

Acknowledgements

This research was financially supported by National 973 Program of China Grant 2007CB936704, National Science Foundation of China Grant 50772123, Science and Technology Commission of Shanghai Grant 0752nm016, and Shanghai Fundamental Research Grant 05JC14080.

References

[1] Fujishima A, Honda K. Electrochemical photolysis of water at semiconductor electrode. Nature 1972;238:37–8.
[2] Kohtani S, Koshiko M, Kudo A, Tokumura K, Ishigaki Y, Toriba A, et al. Photodegradation of 4-alkylphenols using $BiVO_4$ photocatalyst under irradiation with visible light from a solar simulator. Appl Catal B Environ 2003;46:573–86.
[3] Harada H, Hosoki C, Ishikane M. Sonophotocatalysis of water in a CO_2–Ar atmosphere. J Photochem Photobiol A Chem 2003;160:11–7.
[4] Tokunaga S, Kato H, Kudo A. Selective preparation of monoclinic and tetragonal $BiVO_4$ with scheelite structure and their photocatalytic properties. Chem Mater 2001;13:4624–8.
[5] Long M, Cai W, Cai J, Zhou B, Chai X, Wu Y. Efficient photocatalytic degradation of phenol over $Co_3O_4/BiVO_4$ composite under visible light irradiation. J Phys Chem B 2006;110:20211–6.
[6] Tang J, Zou Z, Ye J. Efficient photocatalytic decomposition of organic contaminants over $CaBi_2O_4$ under visible-light irradiation. Angew Chem Int Ed 2004;43:4463–6.
[7] Hu X, Hu C, Qu J. Photocatalytic decomposition of acetaldehyde and *Escherichia coli* using $NiO/SrBi_2O_4$ under visible light irradiation. Appl Catal B Environ 2006;69:17–23.
[8] Fu H, Pan C, Yao W, Zhu Y. Visible-light-induced degradation of rhodamine B by nanosized Bi_2WO_6. J Phys Chem B 2005;109:22432–9.
[9] Zhang C, Zhu Y. Synthesis of square Bi_2WO_6 nanoplates as high-activity visible-light-driven photocatalysts. Chem Mater 2005;17:3537–45.
[10] Shimodaira Y, Kato H, Kobayashi H, Kudo A. Photophysical properties and photocatalytic activities of bismuth molybdates under visible light irradiation. J Phys Chem B 2006;110:17790–7.
[11] Kudo A, Hijii S. H_2 or O_2 evolution from aqueous solution on layered oxide photocatalysts consisting of Bi^{3+} with $6s^2$ configuration and d^0 transition metal ions. Chem Lett 1999;28:1103–4.
[12] Yao WF, Wang H, Xu XH, Zhou JT, Yang XN, Zhang Y, et al. Photocatalytic property of bismuth titanate $Bi_2Ti_2O_7$. Appl Catal A Gen 2004;259:29–33.
[13] Yao WF, Xu XH, Wang H, Zhou JT, Yang XN, Zhang Y, et al. Photocatalytic property of perovskite bismuth titanate. Appl Catal B Environ 2004;52:109–16.
[14] Gurunathan K. Photocatalytic hydrogen production using transition metal ions-doped γ-Bi_2O_3 semiconductor particles. Int J Hydrogen Energy 2004;29:933–40.
[15] Lin X, Huang F, Wang W, Shi J. Photocatalytic activity of $Bi_{24}Ga_2O_{39}$ for degrading methylene blue. Scripta Mater 2007;56:189–92.
[16] Lin X, Huang F, Wang W, Xia Y, Wang Y, Liu M, et al. Photocatalytic activity of a sillenite-type material $Bi_{25}GaO_{39}$. Catal Commun 2007;8:1767–71.
[17] Wang J, Zou Z, Ye J. Surface modification and photocatalytic activity of distorted pyrochlore-type Bi_2M(M = In, Ga and Fe)TaO_7 photocatalysts. J Phys Chem Solids 2005;66:349–55.
[18] Zou Z, Ye J, Sayama K, Arakawa H. Photocatalytic and photophysical properties of a novel series of solid photocatalysts, $BiTa_{1-x}Nb_xO_4$ ($0 \le x \le 1$). Chem Phys Lett 2001;343:303–8.
[19] Zou Z, Ye J, Arakawa H. Photocatalytic and photophysical properties of a novel series of solid photocatalysts, Bi_2MNbO_7 (M = Al^{3+}, Ga^{3+} and In^{3+}). Chem Phys Lett 2001;333:57–62.
[20] Andersen OK. Linear methods in band theory. Phys Rev B 1975;12:3060–83.
[21] Andersen OK, Jepsen O. Explicit, first-principles tight-binding theory. Phys Rev Lett 1984;53:2571–4.
[22] Jepsen O, Andersen OK. Calculated electronic structure of the sandwich d^1 metals LaI_2 and CeI_2: application of new LMTO techniques. Z Phys B Condens Matter 1995;97:35–47.
[23] Hedin L, Lundqvist BI. Explicit local exchange-correlation potentials. J Phys C Solid State Phys 1971;4:2064–83.
[24] Lambrecht WRL, Andersen OK. Minimal basis sets in the linear muffin-tin orbital method: application to the diamond-structure crystals C, Si, and Ge. Phys Rev B 1986;34:2439–49.
[25] Jepsen O, Andersen OK. The electronic structure of h.c.p. ytterbium. Solid State Commun 1971;9:1763–7.
[26] Löwdin PO. A note on quantum-mechanical perturbation theory. J Chem Phys 1951;19:1396–401.
[27] Bradley CJ, Cracknell AP. The mathematical theory of symmetry in solids. Oxford: Clarendon Press; 1972.
[28] Herrmann JM, Tahiri H, Ait-Ichou Y, Lassaletta G, Gonzalez-Elipe AR, Fernandez A. Characterization and photocatalytic activity in aqueous medium of TiO_2 and Ag-TiO_2 coatings on quartz. Appl Catal B 1997;13:219–28.
[29] Nasr C, Vinodgopal K, Fisher L, Hotchandani S, Chattopadhyay AK, Kamat PV. Environmental photochemistry on semiconductor surfaces. Visible light induced degradation of a textile diazo dye, naphthol blue black, on TiO_2 nanoparticles. J Phys Chem 1996;100:8436–42.
[30] Kuo WS, Ho PH. Solar photocatalytic decolorization of dyes in solution with TiO_2 film. Dyes Pigments 2006;71:212–7.
[31] Baiocchi C, Brussino MC, Pramouro E, Prevot AB, Palmisano L, Marci G. Characterization of methyl orange and its photocatalytic degradation products by HPLC/UV–VIS diode array and atmospheric pressure ionization quadrupole ion trap mass spectrometry. Int J Mass Spectrom 2002;214:247–56.
[32] Comparelli R, Fanizzaa E, Curri ML, Cozzoli PD, Mascolo G, Passino R, et al. Photocatalytic degradation of azo dyes by organic-capped anatase TiO_2 nanocrystals immobilized onto substrates. Appl Catal B Environ 2005;55:81–91.
[33] Comparelli R, Fanizzaa E, Curri ML, Cozzoli PD, Mascolo G, Agostiano A. UV-induced photocatalytic degradation of azo dyes by organic-capped ZnO nanocrystals immobilized onto substrates. Appl Catal B Environ 2005;60:1–11.
[34] Badr Y, Mahmoud MA. Photocatalytic degradation of methyl orange by gold silver nano-core/silica nano-shell. J Phys Chem Solids 2007;68:413–9.
[35] Hachem C, Bocquillon F, Zahraa O, Bouchy M. Decolourization of textile industry wastewater by the photocatalytic degradation process. Dyes Pigments 2001;49:117–25.
[36] Dai K, Chen H, Peng T, Ke D, Yi H. Photocatalytic degradation of methyl orange in aqueous suspension of mesoporous titania nanoparticles. Chemosphere 2007. doi:10.1016/j.chemosphere.2007.05.021.
[37] Radaev SF, Simonov VI. Structures of sillenite and atomic mechanisms of their isomorphic substitutions. Sov Phys Crystallogr 1992;37:484–99.
[38] Matjaz V, Danilo S. J Am Ceram Soc 2001;84:2900–12.
[39] Kohno M, Ogura S, Inoue Y. Preparation of $BaTi_4O_9$ by a sol–gel method and its photocatalytic activity for water decomposition. J Mater Chem 1996;6:1921–4.
[40] Kohno M, Ogura S, Sato K, Inoue Y. Properties of photocatalysts with tunnel structures: formation of a surface lattice O-radical by the UV irradiation of $BaTi_4O_9$ with a pentagonal-prism tunnel structure. Chem Phys Lett 1997;267:72–6.
[41] Kohno M, Ogura S, Sato K, Inoue Y. Reduction and oxidation of $BaTi_4O_9$ with a pentagonal prism tunnel structure – effects on radical formation upon UV irradiation and on the activity of $RuO_2/BaTi_4O_9$

photocatalyst for water decomposition. J Chem Soc Faraday Trans 1997;93:2433–7.

[42] Kohno M, Kaneko T, Ogura S, Sato K, Inoue Y. Dispersion of ruthenium oxide on barium titanates ($Ba_6Ti_{17}O_{40}$, $Ba_4Ti_{13}O_{30}$, $BaTi_4O_9$ and $Ba_2Ti_9O_{20}$) and photocatalytic activity for water decomposition. J Chem Soc Faraday Trans 1998;94:89–94.

[43] Zhang KL, Lin XP, Huang FQ, Wang WD. A novel photocatalyst $PbSb_2O_6$ for degradation of methylene blue. J Mol Catal A Chem 2006;258:185–90.

[44] Kudo A, Kato H, Nakagawa S. Water splitting into H_2 and O_2 on new $Sr_2M_2O_7$ (M = Nb and Ta) photocatalysts with layered perovskite structures: factors affecting the photocatalytic activity. J Phys Chem B 2000;104:571–5.

[45] Zou Z, Ye J, Arakawa H. Structural properties of $InNbO_4$ and $InTaO_4$: correlation with photocatalytic and photophysical properties. Chem Phys Lett 2000;332:271–7.

[46] Lin X, Huang F, Wang W, Wang Y, Xia Y, Shi J. Photocatalytic activities of $M_2Sb_2O_7$ (M = Ca, Sr) for degrading methyl orange. Appl Catal A Gen 2006;313:218–23.

[47] Shannon RD. Revised effective ionic radii and systematic studies of interatomic distances in halides and chalcogenides. Acta Crystallogr 1976;A32:751–67.